

Selective Wavelength Enhanced Photochemical and Photothermal H₂ Generation of Classical Oxide Supported Metal Catalyst

Serene Wen Ling Ng, Minmin Gao, Wanheng Lu, Minghui Hong, and Ghim Wei Ho*

Conventional views of constructing simply broadband catalysts for photo-thermal-enhanced catalysis do not realize that without designating photochemical and photothermal conversion to their optimal working spectra can lead to a performance trade-off. Here, spectrally selective designed photoredox and photothermal heating functions of a classical oxide supported metal catalyst are demonstrated, which exhibits markedly improved hydrogen reactivity. While photothermal hydrogen producing catalysis is previously demonstrated, distinctive wavelength dominant redox and thermal phenomena are not studied due to the complex interdependent behavior they exhibit. The exceptionally high H₂ evolution rate of 30.2 mmol g⁻¹ h⁻¹ (≈74 times that of the control sample) is attributed to the nonoverlapped light absorption and undisrupted charge transfer rationales. This study presents a proof-by-existence that spectrally tailored solar utilization strategy is broadly impactful for the hybrid photothermal–photochemical catalysis. Moreover, the spatially decoupled structural configuration may open up discrete parametric control over photoredox and photoheating functionalities.

1. Introduction

Highly efficient catalysts for H₂ generation are receiving great research interest due to its potential applications in green and sustainable energy generation.^[1] However, critical bottlenecks of photocatalytic materials encountered in photocatalytic H₂ generation include sluggish charge transfer dynamics^[2] and narrowband light response.^[3] To date, diverse strategies have been implemented to overcome the aforementioned limitations such as cocatalyst incorporation,^[2b,c,4] dye sensitization,^[5] single atom catalysis,^[6] Z-scheme,^[7] and type II photocatalyst, etc.^[8] These strategies aim to broaden the light absorption from

the conventional UV to the visible region and improve charge transfer pathway for efficient charge separation. However, the limitations of the above techniques lie in the restricted utilization of the solar spectrum especially in the NIR region (≈44% of the solar spectrum), which has insufficient energy (minimal energy requirement ≈ 1.5–2.0 eV) to execute photogeneration of H₂.^[9]

In view of this constraint, recent progress in photothermal-enhanced catalysis is an alternative approach to fully harvest and exploit the solar spectrum even in the NIR region.^[10] Suitable photothermal materials include noble metal nanoparticles which demonstrate localized surface plasmon resonance (LSPR) effect,^[11] or semiconductor which exhibits broad light absorption range have largely been used in photothermal-enhanced catalysis.^[3a] To further enhance the photoredox reaction,

cocatalyst such as noble metals^[12] or semiconductors^[13] with suitable energy levels are often added as active sites. Although photothermal-enhanced catalysis generally seems to be effective, there are overlooked or undisclosed challenges to fully exploit solar power for the photothermal catalytic technology to operate at its highest catalytic efficacy and energy conversion efficiency. More often than not, similar materials (mostly metal or semiconductors) for both photothermal and cocatalyst materials are simply blended in an attempt to observe enhanced photothermal catalysis, not knowing that they have given rise to unintended adverse interactions between the added components. The various pitfalls of having similar materials compositions with hybridized photochemical and photothermal functions in a photothermal-enhanced catalyst system are: (i) overlapping of the light absorption spectrum resulting in poor light activation in the photothermal and/or the cocatalyst materials for respective localized heating and charge generation, hence leading to trade off performance; (ii) disruption of the charge transfer pathway of the photocatalyst to cocatalyst due to the incorporation of the photothermal material; and (iii) indistinguishable dominant role of each material constituents, hence inability to optimize the associated photoredox and photothermal effects. Thus, the incorporation of multimaterials into a unitary photocatalyst configuration for efficient full solar spectrum catalysis with maximized dual photochemical and photothermal effects is particularly challenging.

Dr. S. W. L. Ng, Dr. M. Gao, Dr. W. Lu, Prof. M. Hong, Prof. G. W. Ho
Department of Electrical and Computer Engineering
National University of Singapore
4 Engineering Drive 3, Singapore 117583, Singapore
E-mail: elehwg@nus.edu.sg

Prof. G. W. Ho
Institute of Materials Research and Engineering
A*STAR (Agency for Science Technology and Research)
3 Research Link, Singapore 117602, Singapore

 The ORCID identification number(s) for the author(s) of this article can be found under <https://doi.org/10.1002/adfm.202104750>.

DOI: 10.1002/adfm.202104750

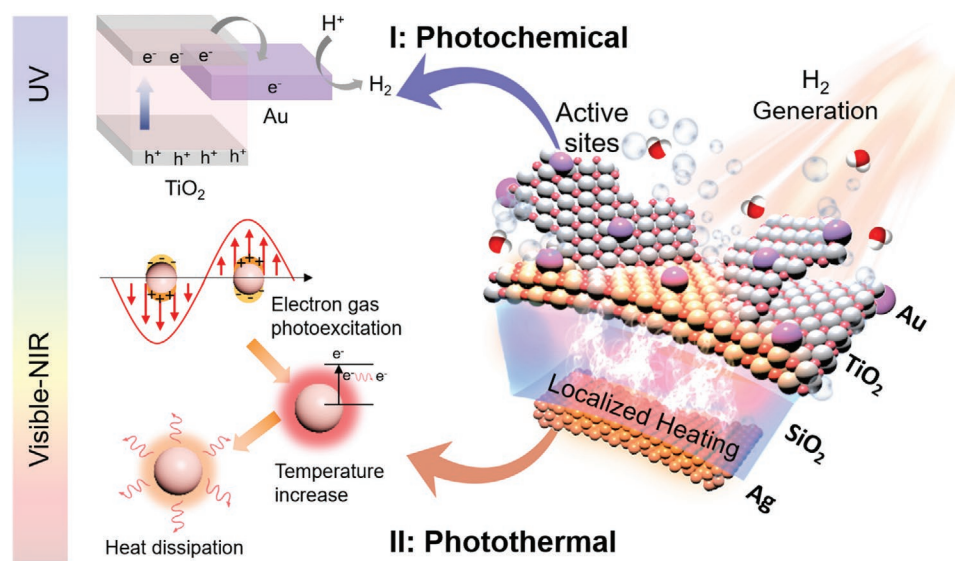


Figure 1. Schematic diagram which illustrates the mechanism for enhanced photocatalytic H₂ generation due to photothermal and photochemical effects.

While photothermal hydrogen producing catalysis was earlier demonstrated, in this work we focus on examining the intermodal wavelength dominant mechanisms that are not easily studied due to the interdependent reactivities and effects they exhibit. Here, we experimentally demonstrate selectively enhanced solar wavelength conversion into photochemical and photothermal modes of hydrogen evolution photocatalysis enhancement using classical oxide supported metal catalyst that is most extensively investigated for catalysis. In order to optimize solar energy utilization, a spatially separated catalysts is designed such that (i) TiO₂/Au nanosheets shell is predominately designated for high energy photon (UV) for enhanced photoredox reaction while (ii) Ag/SiO₂ core is set apart for low energy photon (vis–NIR) utilization to mediate the photothermal effect. The selective enhancement is made possible via the harmonious design of decoupled photothermal and photochemical catalyst such that the partaking mechanisms can be congruently operated in parallel and the catalysis performance is appreciably consequential. The photocatalyst demonstrates superior H₂ production rate of 30.2 mmol g^{−1} h^{−1} and an overall enhancement of ≈74 times compared to the control sample SiO₂@TiO₂, exceedingly better than the reported work.^[14] Notably, the wavelength-selective photothermal-enhanced catalysis, i.e., solar promoted photocatalysis and solar induced thermal catalysis manifests structural and functional decoupled configuration which possibly open up explicit parametric control of photoredox reaction, and additional control over photothermal functionalities.

2. Results and Discussion

The structural design of the hybridized photocatalyst for enhanced photocatalytic H₂ generation after careful considerations is as illustrated in **Figure 1**. Ag@SiO₂ (AS) photothermal core is designed for high photo-to-heat conversion efficiency as Ag exhibits LSPR effect, while the SiO₂ layer enhances the light absorption capabilities due to the change in refractive index

of the surrounding medium around the Ag NPs^[15] for broadband utilization of the solar spectrum. Next, TiO₂ nanosheet (TiO₂ NS) photocatalyst is grown on the as-synthesized photothermal core due to its high surface area and increased active facets which is desirable for enhanced photocatalytic activity. As the localized heating decreases with distance, the core–shell structure is specially designed to keep the photothermal core in close proximity to the TiO₂ photocatalyst, thus maximizing the effect of local heating on the active reaction sites on TiO₂. Lastly, cocatalyst (Au) is introduced by surface loading such that it can be in direct contact with TiO₂ for enhanced photoredox reaction. The photothermal (Ag@SiO₂), photocatalyst (TiO₂), and cocatalyst (Au) are carefully chosen such that Ag@SiO₂ is intended for broadband light absorption (vis–NIR) while TiO₂/Au is responsible for the generation of charge carrier under UV irradiation. It is ensured that the light absorption of the Au does not hinder the light absorption of Ag@SiO₂ (AS) such that the localized heating effect can be maximized. Furthermore, to ensure that the charge transfer pathway of the TiO₂/Au is not compromised with the addition of Ag, the SiO₂ layer also serves the purpose of minimizing the direct contact of Ag and TiO₂/Au. This allows the dominant role of each material constituents to be differentiable, thus optimizing the associated photoredox and photothermal effects. Therefore, the current structural design is desirable for simultaneous realization of photothermal-enhanced catalysis with reduced charge recombinations for enhanced photocatalytic H₂ generation.

Figure S1a in the Supporting Information shows the scanning electron microscope (SEM) image of the photothermal core (AS), where the core–shell structure is revealed with Ag NP in the centre of the SiO₂ spheres, which indicates the successful coating of SiO₂ around the Ag NPs. The presence of the Ag core was also confirmed with transmission electron microscope (TEM) (**Figure 2a**), where dark spots were seen in the centre of the SiO₂ spheres. Enhanced light absorption with peak at 400 nm can be observed (**Figure 2b**) which is accredited to the LSPR effect of Ag, induced by the surface oscillations of

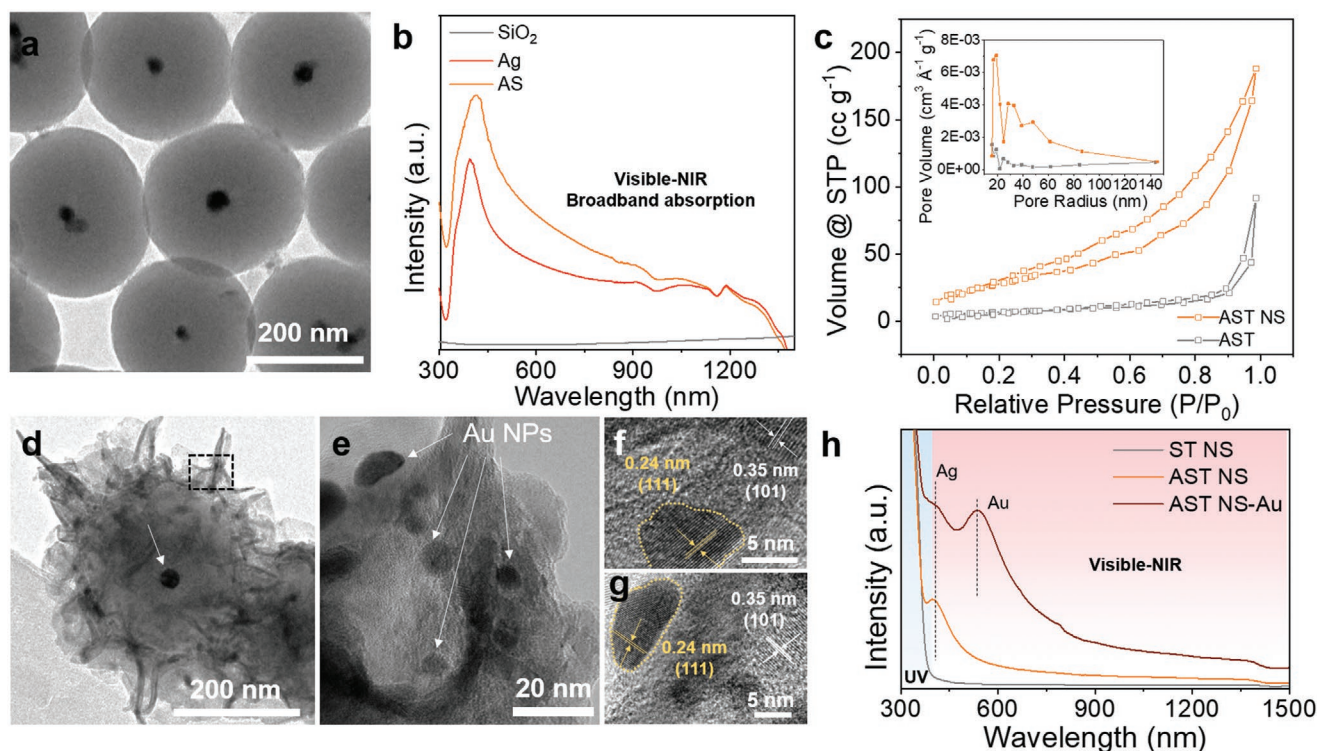


Figure 2. TEM image of a) Ag@SiO₂ (AS), b) UV-vis spectrum of SiO₂, Ag, and AS, c) N₂ adsorption-desorption isotherm and pore size distribution curves (inset) of AST and AST NS, d) TEM images of AST NS-Au e-g) high resolution TEM images of AST NS-Au, h) UV-vis spectrum of ST NS, AST NS, and AST NS-Au.

conduction band electrons.^[16] Due to incorporation of the SiO₂ shell, broadened and enhanced light absorption were observed (Figure 2b). This is attributed to the difference in refractive index of the core and shell, which possesses light trapping configuration that boosts light absorption capabilities.^[17] This enhancement indicates more photons can be turned to heat, which can further accelerate the holes scavenging process, increasing the number of electrons available for photocatalytic H₂ generation.^[18] X-ray powder diffraction (XRD) was also performed which further confirms the presence of the Ag NPs (Figure S1b, Supporting Information). The diffraction peaks of Ag were observed at 38.2°, 44.4°, 64.6°, 77.6°, and 81.7° (JCPDS No. 4-0783).^[19]

TiO₂ NS was grown on the AS for close interfacial contact of the photothermal and photocatalytic materials which maximizes the effect of localized heating on the TiO₂ active sites. Additionally, the role of the SiO₂ layer acts as a barrier to prevent charge transfer from TiO₂ to Ag. Figure S2a in the Supporting Information reveals the SEM image of Ag@SiO₂@TiO₂ NS (AST NS), where nanosheets are seen conforming around AS. AST NS was then compared to (Ag@SiO₂@TiO₂) AST (Figure S2b, Supporting Information) to ascertain the effect of increased surface area, porosity and active facets on the photocatalytic performance. The percentage of exposed {001} active facets which is important for efficient photocatalytic activity can be inferred from the XRD results (Figure S3a, Supporting Information). The broader {004} diffraction peak of AST NS suggests the reduction in size along the (001) axis, while the enhanced intensity of the (101) peak is attributed to an enlarged crystallite size along the (101) axis.^[20] Both results

indicate the enhancement in percentage of {001} facets in AST NS.^[20] The surface area of AST and AST NS were measured using BET (Figure 2c), and were found to be 23.7 and 105.2 m² g⁻¹, respectively. The analysis also indicated that AST NS exhibited higher porosity compared to AST (Figure 2c inset). The increase in active facets, surface area, and porosity are favorable for boosting the photocatalytic performance due to an increased number of active reaction sites present. Additionally, the high porosity and surface area also facilitate the penetration of reactants to the TiO₂, thus increasing the interaction of reactant and photocatalyst for redox reactions to occur. Therefore, under UV irradiation, AST NS demonstrated higher photocatalytic performance with H₂ production rate of 1.18 mmol g⁻¹ h⁻¹, compared to AST of 0.38 mmol g⁻¹ h⁻¹ (Figure S3b, Supporting Information).

Au NPs were subsequently loaded on AST NS for the investigation of cocatalyst effect of Au on H₂ production rate. Importantly, the cocatalyst is selected such that its light absorption peak does not coincide with the photothermal core, thus fully maximizing the light absorption capabilities of the photothermal core (AS). SEM (Figure S4, Supporting Information) and TEM (Figure 2d) images of AST NS-Au reveal the core-shell structure of AST NS. Such core-shell structure is known to be beneficial for photocatalytic reaction due to increased interfacial contact of the photothermal core and the photocatalytic material, thereby enhancing localized heating near the active sites of TiO₂/Au. Au NPs distributed on the AST NS surface can be seen under high-resolution imaging (Figure 2e). Figure 2f,g indicates the lattice fringe of TiO₂ with *d*-spacing of 0.35 nm and the presence of Au NPs with *d*-spacing of 0.24 nm.

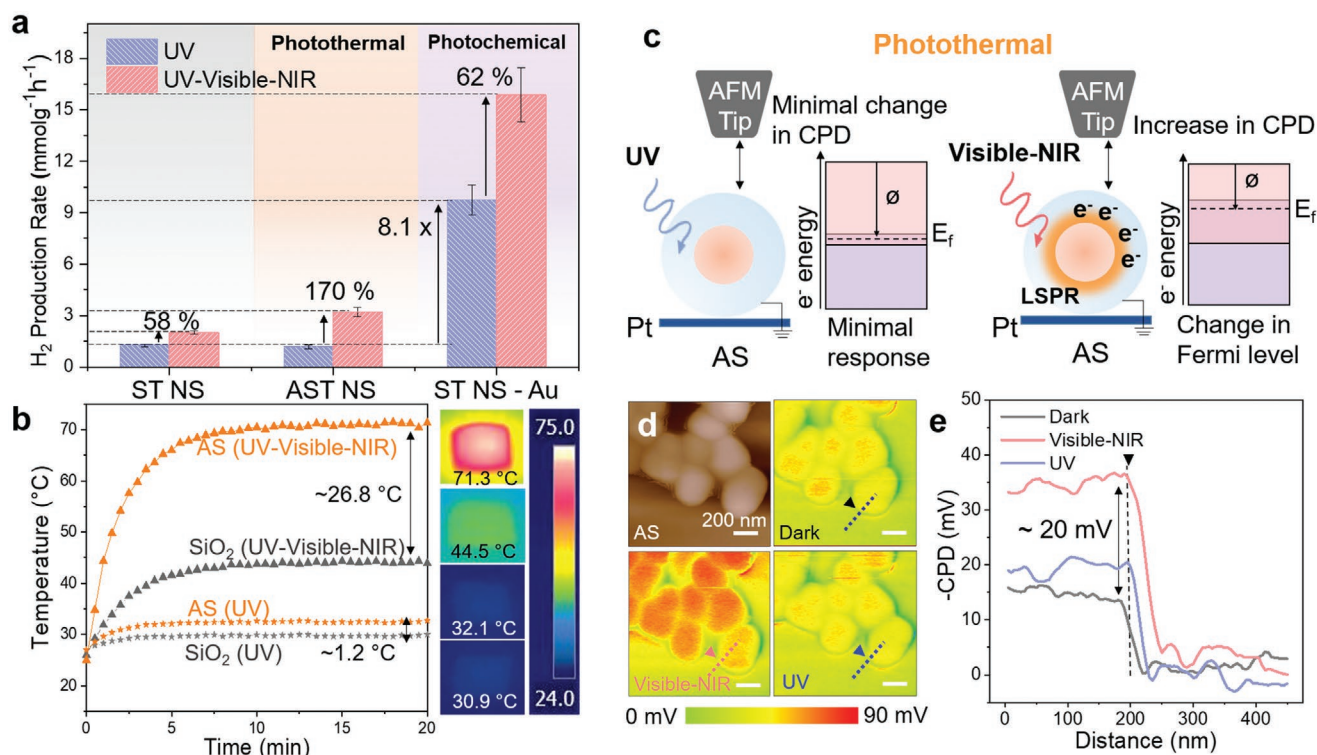


Figure 3. a) H₂ generation rates of ST NS, AST NS, and ST NS-Au under UV and full spectrum irradiation, b) temperature profile of SiO₂ and AS under UV and full spectrum irradiation, c) schematic diagram of the effect of UV and Vis-NIR irradiation on the surface potential in AS, d) topography and the inverse contact potential difference (-CPD) of AS, and e) line profiles of -CPD along lines marked in d) under various light source illumination.

The XRD spectra also shows the presence of TiO₂ in anatase phase (JCPDS no. 21-1272) and Ag with peaks corresponding to (111), (200), and (220) planes (JCPDS no. 04-0783) (Figure S1b, Supporting Information). Importantly, the UV-vis absorption spectrum of AST NS shows a broad peak at ≈400 nm which is attributed to the LSPR effect of the AS core (Figure 2h) while the LSPR peak of Au was observed at ≈550 nm. The distinct absorption peaks of Ag and Au are intended such that the photothermal effect of AS is not compromised due to light shielding.

Next, the photothermal effect of Ag on the photocatalytic activity were validated. SiO₂@TiO₂ NS (ST NS) (Figure S5, Supporting Information) was used as the control sample to ascertain the dominant role of Ag in the photocatalytic H₂ generation process. The H₂ production rates of both samples were measured under UV illumination, ST NS and AST NS produce H₂ at a rate of 1.26 and 1.18 mmol g⁻¹ h⁻¹, respectively (Figure 3a). The increase in H₂ generation after the incorporation of Ag in this case is small (≈11%) as Ag is expected to have negligible contribution as an electron sink due to the insulated SiO₂ layer, which prevents any charge transport from TiO₂ to Ag. The photothermal effect on H₂ generation rates were studied with an addition of a vis-NIR light source. The increments of H₂ generation rate from UV to full spectrum (UV-vis-NIR) are ≈58% and ≈170% for ST NS and AST NS, respectively (Figure 3a). To affirm that the increment in H₂ generation is due to the localized photothermal heating effect and to differentiate it from bulk heating, the reaction solution was kept at a fixed temperature of 50 °C, which is the highest attainable temperature by

AST NS under full spectrum irradiation (Figure S6a, Supporting Information). The setup utilized is illustrated in Figure S6b in the Supporting Information. Having kept the temperature constant, ST NS exhibited nominal difference (≈1.3%) in the H₂ production rate compared to AST NS, upon the addition of vis-NIR irradiation. This suggests that SiO₂ alone has minimal contribution to the localized heating effect under vis-NIR irradiation and thus, the increment observed in ST NS (Figure 3a) is accredited to bulk heating. In contrary, an enhancement of ≈37.5% in the H₂ production rate from 0.81 to 1.10 mmol g⁻¹ h⁻¹ was observed in AST NS (Figure S6c, Supporting Information), which affirms that the H₂ enhancement observed in Figure 3a is ascribed to the localized heating effect of AS, not due to the effect of increased temperature of bulk solution alone. The localized heating around the AS nanoparticles are known to facilitate the hole scavenging process on the active sites of the photocatalytic material, thus improving the H₂ generation rate.^[21] This is further supported by photocurrent measurements (Figure S7, Supporting Information), where a noticeable decrease in photocurrent (≈11%) is observed in AST NS under UV and full spectrum irradiation, compared to ST NS of ≈2.4%. This suggests that due to the localized heating of Ag in AST NS, the hole-scavenging effect on the active sites of TiO₂ NS is accelerated, as such, more electrons are available to be utilized to generate H₂ gas. This reduces the number of electrons flowing to the FTO electrode, resulting in a photocurrent drop.

To further affirm that the huge increment in H₂ generation rate is attributed to the photothermal effect of AS, indicating that the major contribution in the improved H₂ production rate

is resulting from the conversion of vis–NIR photon to heat. Temperature profile measurements of SiO₂ and AS under UV and full spectrum irradiation were demonstrated (Figure 3b). After 20 min of UV irradiation, the bulk temperature of powdered AS reached ≈32.1 °C, while that of SiO₂ reached ≈30.9 °C, indicating that Ag has minimal contributions to heat under UV irradiation (difference of ≈1.2 °C), which is in agreement with the H₂ production results. SiO₂ and AS exhibited similar trend in liquid under UV irradiation, with temperature difference of ≈0.9 °C (Figure S8, Supporting Information). Subsequently, full spectrum light was used and the temperature increased drastically especially in AS sample. AS reached a high temperature of ≈71.3 °C while SiO₂ only achieved temperature of ≈44.5 °C. Notably, a difference of ≈26.8 °C was realized under full spectrum irradiation, which can be attributed to localized heating around the nanoparticles due to the LSPR effect of Ag. The temperature difference of SiO₂ and AS in liquid also exhibited a difference of ≈3.5 °C (Figure S8, Supporting Information). When irradiating Ag NPs with vis–NIR light, free electrons on the nanoparticle surface are excited and conduction-band electrons collectively oscillate to strongly absorb the incident light. The absorbed photons either decay nonradiatively which results in localized heating or decay radiatively by reemission of light.^[22] As schematically shown in Figure 3c, the generation of hot electrons under vis–NIR irradiation increases the number of free electrons, resulting in the upward shift of Fermi level and a decrease in work function; while these changes do not appear under UV (365 nm) irradiation as the wavelength does not match with the LSPR peak of Ag NPs. Thus, determining the light-induced variations in work function promises an effective approach to visualize the LSPR-induced hot electron generation, which is the origin of the localized heating effect. To demonstrate the localized heating effect of AS, KPFM equipped with different light sources were employed to determine the light-induced variations in work function by measuring changes in contact potential difference (CPD)^[23]

$$\text{CPD} = (\phi_{\text{tip}} - \phi_{\text{sample}}) / -e \quad (1)$$

where ϕ_{tip} and ϕ_{sample} are the work functions of tip and sample, respectively; and e is the electronic charge.

Figure 3d,e is the maps and line profiles of the inverse CPD (-CPD) of AS in dark, illuminated under vis–NIR (400–1100 nm) or UV light (365 nm). The broad vis–NIR light illumination causes a significant increase in -CPD (≈20 mV) compared to that in the dark condition, while UV light illumination only change the -CPD marginally (≈4 mV). According to Equation (1), given that the work function of the Pt-coated tip (ϕ_{tip}) is kept constant, an increase in CPD implies a decrease in ϕ_{sample} , suggesting an increase of electron density due to the LSPR effect in Ag NPs under vis–NIR light irradiation (Figure 3c). Thus, validating that more hot electrons are generated in Ag under vis–NIR light which is favorable for the photothermal effect. Noting that -CPD can be also altered due to the surface charge variations from photoexcitation, the -CPD of SiO₂ was also measured under the different light conditions. In this case, the -CPD remain relatively similar (≈15 mV) under all conditions. Thus, this implies that the photoexcitation-induced surface charge generation due to SiO₂ can be excluded in AS (Figure S9,

Supporting Information). Therefore, the KPFM results in combination with the temperature profiles and H₂ generation results, reveal that the dominant role of Ag@SiO₂ in improving the H₂ generation rate is the high photon-to-heat (photothermal) conversion with the addition of vis–NIR light irradiation.

Moving on, the cocatalyst effect of Au on ST NS was also investigated. From the H₂ generation results (Figure 3a), the H₂ production rate of ST NS-Au increases drastically under UV irradiation, ≈8.1 times more than that of ST NS. This increment is attributed to Au acting as an electron sink, drawing electrons away from TiO₂ NS to facilitate the photoredox H₂ generation. Moreover, since Au also exhibits LSPR effect with absorption peak at 550 nm, the increment in H₂ generation with the addition of vis–NIR light was also investigated. Notably, an enhancement in the H₂ generation rate of ≈62% under UV and full spectrum were demonstrated (Figure 3a). The increment was similar to ST NS (≈58%), which implies that the enhancement in ST NS-Au with the addition of vis–NIR light is also due to the bulk heating effect instead of the photothermal effect as discussed previously.

The bulk temperature of ST NS and ST NS-Au powder were measured under UV and full spectrum irradiation (Figure 4a). After 20 min of UV irradiation, the bulk temperature of ST NS and ST NS-Au powder were found to reach ≈32 °C with slight variations from each other (±1 °C). Subsequently, full spectrum was utilized and the maximum temperature attainable increased for both samples, with ST NS-Au displaying a temperature of ≈11 °C more than that of pure ST NS. Although the temperature difference may suggest localized heating due to the Au NPs, there is negligible change (≈1.4%) in the photocurrent obtained for ST NS-Au (Figure 4b), under UV and full spectrum irradiation, suggesting that the temperature increase observed is due to bulk heating instead of localized heating. The dominant role of Au in H₂ generation is further analyzed with KPFM (Figure 4c). Figure 4d presents the topography and maps of the inverse CPD (-CPD) of ST NS-Au deposited on a Pt-coated silicon substrate under dark, UV, and vis–NIR irradiation. Compared to -CPD in the dark, UV irradiation results in an obvious -CPD increase of ≈10 mV while vis–NIR irradiation shows a comparable value (variation < ≈1 mV) (Figure 4e). The minimal change in -CPD of ST NS-Au between dark and vis–NIR indicate that the generation of hot electrons is negligible to result in a change in electron density and the consequent shift in Fermi level of Au NPs. On the other hand, the change in -CPD under UV irradiation is attributed to the charge accumulation on the sample. According to the CPD definition ($\text{CPD} = V_{\text{tip}} - V_{\text{sample}}$), the -CPD increase signifies the increase in sample's potential (V_{sample}), given that the tip's potential (V_{tip}) does not change. The V_{sample} increase implies an accumulation of positive charges over the sample's surface, that is, the hole accumulation over ST NS-Au. As illustrated in Figure 4c, electron–hole pairs are generated under UV irradiation due to photoexcitation of TiO₂; as a result of a larger work function of Au compared to TiO₂, these electrons tend to transfer to Au and then be grounded by the Pt coating on the substrate, resulting in the accumulation of holes and the consequent -CPD increase. Without Au, the increase in the -CPD of ST NS under UV irradiation is half (≈5 mV) of ST NS-Au (Figure S10, Supporting Information). Therefore, the

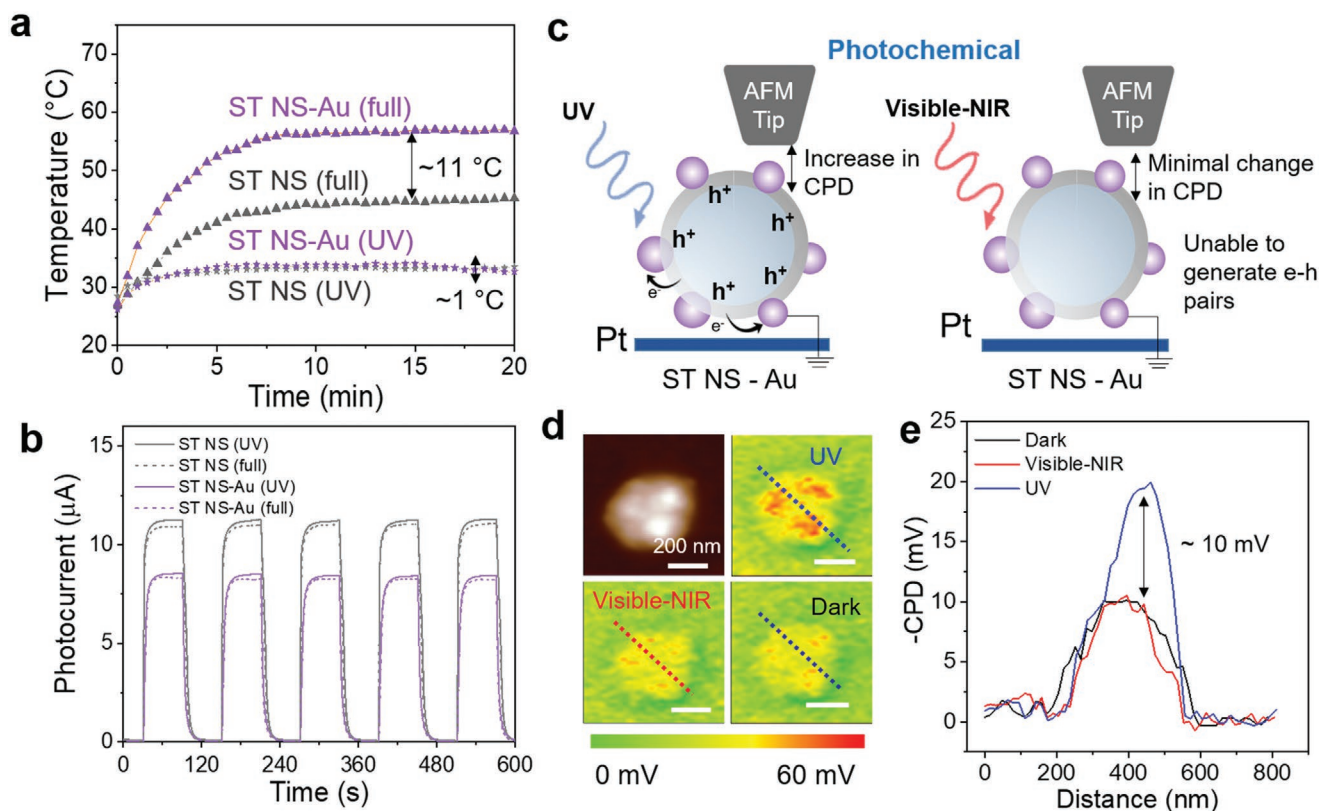


Figure 4. a) Temperature profile, b) photocurrent of ST NS and ST NS-Au under UV and full spectrum irradiation, c) schematic diagram of the effect of UV and vis-NIR irradiation on the surface potential in ST NS-Au, d) topography and the inverse contact potential difference (-CPD) of ST NS-Au and e) line profiles of -CPD along lines marked in d) under various light source illumination

above results confirm that the dominant role of Au is to create a charge transport pathway that promotes the photocatalytic reaction instead of the photothermal effect that accelerates the hole scavenging effect.

Lastly, these two systems were hybridized to form AST NS-Au and H₂ measurements were taken under UV and full spectrum illumination to investigate the integrated cocatalyst and photothermal effect. Expectedly, the incorporation of Au NPs resulted in an increase in H₂ generated under UV illumination (Figure 5a). The optimal Au loading amounts was found and the H₂ production rate is 14.0 mmol g⁻¹ h⁻¹, ≈11 times that of ST NS (Figure S11, Supporting Information). These improvements are attributed to the presence of Au, which facilitated the charge transport from TiO₂ to the metal nanoparticles as proven earlier. On the other hand, the increment in the H₂ generation of AST NS-Au samples from UV to full spectrum are ≈126%, 114%, and 106% for 3, 5, and 7 wt%, respectively (Figure S11, Supporting Information). Although there is a decrease in the photothermal increment in H₂ generation compared to AST NS (≈170%) which may be attributed to the slight overlapping of light absorption of Au and Ag NPs at 400 nm (Figure 2h), the increments of the H₂ generation are all above 100%, much higher than the increment observed in ST NS-Au (≈62%) (Figure 3a), suggesting that the photothermal effect of Ag is still prominent in this case. This is attributed to the distinct absorption peak of both Ag (400 nm) and Au NPs (550 nm) materials which assists the concept of minimal

overlapping light absorption, such that the localized photothermal heating capabilities of Ag can be preserved.

In addition, the cocatalyst effect of Au in this case was not compromised due to the encapsulation of Ag NPs, preventing contact with the photocatalytic and cocatalyst material. In order to further examine the dual photothermal and cocatalyst effect of Ag and Au, respectively, various single wavelength visible/NIR light sources are utilized and H₂ generation rates are measured. Figure 5b reveals the H₂ production rate of AST NS-Au under UV (365 nm) alone, with visible/NIR light sources at different wavelengths. The largest increment in H₂ generation at 400 nm matches the resonance peak of Ag NPs (400 nm) where an enhancement of ≈75.0% was demonstrated. Conversely, at higher wavelengths of 450, 500, and 550 nm, the enhancement in H₂ generation decreases to ≈44.7%, ≈49.4%, and ≈36.9%, respectively. Nevertheless, these enhancements are attributed to the localized heating effect of Ag due to the broad light absorption capabilities. At wavelength of 600 to 700 nm, there were no increment observed as the light absorption (Figure 5b) is ascribed to the Au NPs instead of Ag. Thus, this further affirms that the dominant role of Au NPs is for enhanced charge transfer pathway instead of the photothermal effect that accelerates hole scavenging.

As the stability of the photocatalyst is important in establishing the efficiency of the photocatalyst, the photocatalytic performance of AST NS with 5 wt% Au NPs under UV and full spectrum were investigated for four cycles. The H₂ production

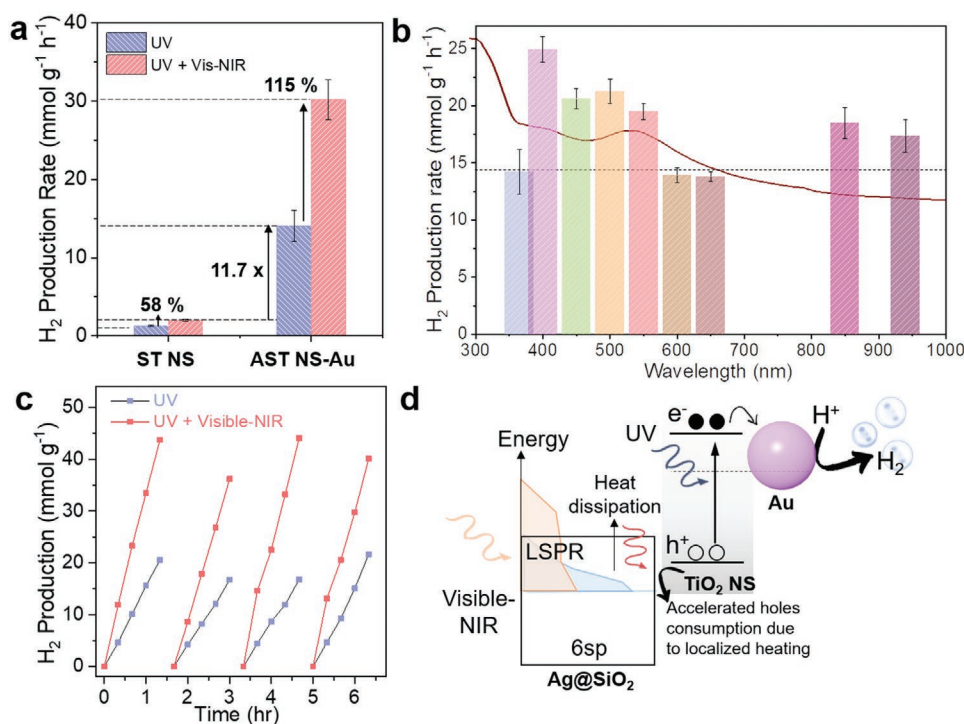


Figure 5. a) H₂ production rates of ST NS and AST NS-Au under UV and full spectrum irradiation, b) H₂ production rates of AST NS-Au under UV ($\lambda = 365$ nm) and with addition of different wavelength irradiation (vis-NIR, $\lambda \geq 400$ nm). c) H₂ production stability of AST NS-Au. d) Mechanism of the synergistic photothermal and photochemical effect on H₂ generation.

for both UV and full spectrum remained relatively stable with H₂ generation rates of 14.0 ± 1.9 and 30.2 ± 2.5 mmol g⁻¹ h⁻¹, respectively as shown in Figure 5c. The H₂ production rate, compared to the control sample (ST) is ≈ 74 times higher (Figure S12, Supporting Information), which is relatively high with reference to recent works (Table S1, Supporting Information). The mechanism for the boosted photocatalytic H₂ generation is illustrated as shown in Figure 5d. First, Ag is designed to absorb visible light for efficient light-to-heat conversion, while the SiO₂ layer increases the overall light absorption capabilities and simultaneously minimizes the contact of Ag with TiO₂/Au. Second, TiO₂ NS is the photocatalyst responsible for the generation of electron-hole pairs for H₂ generation under UV illumination. Lastly, the addition of Au NPs on TiO₂ surface acts as cocatalyst for efficient charge transfer. Therefore, photogenerated electrons in TiO₂ NS under UV irradiation (Figure 5di) are transported to the Au NPs due to the large work function of Au. This transfer of electrons greatly reduces the fast charge recombination in TiO₂, which increases the number of electrons available for H₂ generation. Next, with the addition of the vis-NIR light illumination, the Ag@SiO₂ exhibited LSPR effect (Figure 5dii). The hot electrons generated due to the LSPR effect can either decay through photons re-emission, or through nonradiative decay via electron-electron interactions. In nonradiative decay, the hot carriers collide with other electrons in metal, thus transferring their energy to the neighboring electrons.^[10b,24] The high energy electrons then collide with the ionic lattice of the metal nanoparticles (electron-phonon coupling),^[24a] which results in a rise in the local temperature of the metal nanoparticles. Eventually, the heat is

transferred from the metal to TiO₂ due to the coupled vibration of both the metal and TiO₂ (phonon-phonon coupling).^[25] This confined heat produced results in an increase in the localized temperature of the photocatalyst.^[10a,b] Thus, aiding in the acceleration of redox reaction of the hole-scavenging glycerol (Figure 5di).^[3a,21] As such, the number of available electrons on the photocatalyst increases further, resulting in more H₂ gas being generated.

3. Conclusion

Photocatalyst with dual effect of enhanced charge transfer and photothermal heating for boosted H₂ generation has been demonstrated. The photocatalyst exhibited exceptionally high H₂ generation rate of 30.2 mmol g⁻¹ h⁻¹ which is ≈ 74 times that of ST. The high H₂ performance is ascribed to the designed AST NS-Au NPs core-shell structure for effectual utilization of the solar energy, where UV light is utilized for the electron-hole pairs generation in TiO₂ for H₂ generation and AS absorbs visible light for efficient photo-to-heat conversion. The number of active sites for photocatalytic reactions is boosted due to the increase in the active facets, surface area and porosity in TiO₂ NS. The addition of Au NP reduces the charge recombination in TiO₂, which further improves the photocatalytic performance. Moreover, the Au NPs (cocatalyst) showed suitability to be used in conjunction with Ag NPs (photothermal), as they each exhibit light absorption at different wavelengths. Therefore, this facile hybrid design of photochemical and photothermal effect are proven to be feasible. In general, the

approaches demonstrated in this study could potentially pave the pathway and open new doors for the development of other photocatalytic material designs which can be expected to be useful in the field of energy generation and sustainability.

Supporting Information

Supporting Information is available from the Wiley Online Library or from the author.

Acknowledgements

This research was supported by A*STAR under its 2019 AME IRG & YIRG Grant Calls, A2083c0059.

Conflict of Interest

The authors declare no conflict of interest.

Data Availability Statement

Research data are not shared.

Keywords

H₂ production, photocatalysis, photochemical, photothermal

Received: May 19, 2021

Revised: June 18, 2021

Published online: July 2, 2021

- [1] a) A. Alarawi, V. Ramalingam, H.-C. Fu, P. Varadhan, R. Yang, J.-H. He, *Opt. Express* **2019**, *27*, A352; b) A. Manikandan, P. R. Ilango, C.-W. Chen, Y.-C. Wang, Y.-C. Shih, L. Lee, Z. M. Wang, H. Ko, Y.-L. Chueh, *J. Mater. Chem. A* **2018**, *6*, 15320; c) A. Manikandan, L. Lee, Y.-C. Wang, C.-W. Chen, Y.-Z. Chen, H. Medina, J.-Y. Tseng, Z. M. Wang, Y.-L. Chueh, *J. Mater. Chem. A* **2017**, *5*, 13320.
- [2] a) Q.-F. Liu, Q. Zhang, B.-R. Liu, S. Li, J.-J. Ma, *Chin. J. Catal.* **2018**, *39*, 542; b) Z. Zhu, C.-T. Kao, B.-H. Tang, W.-C. Chang, R.-J. Wu, *Ceram. Int.* **2016**, *42*, 6749; c) L. Kong, J. Yan, S. F. Liu, *ACS Sustainable Chem. Eng.* **2019**, *7*, 1389; d) S. W. L. Ng, M. Gao, W. L. Ong, K. Lim, C. Peh, G. Ho, *J. Mater. Chem. A* **2018**, *6*, 16213.
- [3] a) M.-Q. Yang, L. Shen, Y. Lu, S. W. Chee, X. Lu, X. Chi, Z. Chen, Q.-H. Xu, U. Mirsaidov, G. W. Ho, *Angew. Chem., Int. Ed.* **2019**, *58*, 3077; b) L. Guo, Z. Yang, K. Marcus, Z. Li, B. Luo, L. Zhou, X. Wang, Y. Du, Y. Yang, *Energy Environ. Sci.* **2018**, *11*, 106; c) L. Zhu, M. Gao, C. K. N. Peh, G. W. Ho, *Mater. Horiz.* **2018**, *5*, 323; d) X. Zhang, M. Ge, J. Dong, J. Huang, J. He, Y. Lai, *ACS Sustainable Chem. Eng.* **2019**, *7*, 558.
- [4] F. Xu, K. Meng, B. Zhu, H. Liu, J. Xu, J. Yu, *Adv. Funct. Mater.* **2019**, *29*, 1904256.
- [5] a) Z. Wang, X. Lang, *Appl. Catal., B* **2018**, *224*, 404; b) C. S. Karthikeyan, H. Wietasch, M. Thelakkat, *Adv. Mater.* **2007**, *19*, 1091.
- [6] A. Alarawi, V. Ramalingam, J.-H. He, *Mater. Today Energy* **2019**, *11*, 1.
- [7] a) B.-J. Ng, L. K. Putri, X. Y. Kong, Y. W. Teh, P. Pasbakhsh, S.-P. Chai, *Adv. Sci.* **2020**, *7*, 1903171; b) Y. Wang, X. Shang, J. Shen, Z. Zhang, D. Wang, J. Lin, J. C. S. Wu, X. Fu, X. Wang, C. Li, *Nat. Commun.* **2020**, *11*, 3043.
- [8] a) K. Li, L. Wang, Z. Chen, X. Yang, Y.-X. Yu, W.-D. Zhang, Y. Wang, Y. Shi, K. P. Loh, Q.-H. Xu, *Adv. Funct. Mater.* **2020**, *30*, 2005106; b) Y. Lei, S. Xu, M. Ding, L. Li, Q. Sun, Z. L. Wang, *Adv. Funct. Mater.* **2020**, *30*, 2005716.
- [9] M. G. Walter, E. L. Warren, J. R. McKone, S. W. Boettcher, Q. Mi, E. A. Santori, N. S. Lewis, *Chem. Rev.* **2010**, *110*, 6446.
- [10] a) D. Werner, S. Hashimoto, T. Uwada, *Langmuir* **2010**, *26*, 9956; b) J. A. Webb, R. Bardhan, *Nanoscale* **2014**, *6*, 2502; c) M.-Q. Yang, M. Gao, M. Hong, G. W. Ho, *Adv. Mater.* **2018**, *30*, 1802894.
- [11] a) M. Gao, C. K. Peh, L. Zhu, G. Yilmaz, G. W. Ho, *Adv. Energy Mater.* **2020**, *10*, 2000925; b) P. Sriram, A. Manikandan, F.-C. Chuang, Y.-L. Chueh, *Small* **2020**, *16*, 1904271.
- [12] F. Wang, R. J. Wong, J. H. Ho, Y. Jjiang, R. Amal, *ACS Appl. Mater. Interfaces* **2017**, *9*, 30575.
- [13] S. Akel, R. Dillert, N. O. Balayeva, R. Boughaled, J. Koch, M. El Azzouzi, D. W. Bahnemann, *Catalysts* **2018**, *8*, 647.
- [14] a) A. T. Montoya, E. G. Gillan, *ACS Omega* **2018**, *3*, 2947; b) N. Meng, J. Ren, Y. Liu, Y. Huang, T. Petit, B. Zhang, *Energy Environ. Sci.* **2018**, *11*, 566; c) Y. Yu, W. Yan, X. Wang, P. Li, W. Gao, H. Zou, S. Wu, K. Ding, *Adv. Mater.* **2018**, *30*, 1705060.
- [15] a) T. Pakizeh, *J. Opt.* **2012**, *15*, 025001; b) F. Frederix, J.-M. Friedt, K.-H. Choi, W. Laureyn, A. Campitelli, D. Mondelaers, G. Maes, G. Borghs, *Anal. Chem.* **2003**, *75*, 6894; c) S. Sarina, E. R. Waclawik, H. Zhu, *Green Chem.* **2013**, *15*, 1814.
- [16] K. Shrivastava, S. Sahu, G. K. Patra, N. K. Jaiswal, R. Shankar, *Anal. Methods* **2016**, *8*, 2088.
- [17] E. Ringe, J. M. McMahon, K. Sohn, C. Copley, Y. Xia, J. Huang, G. C. Schatz, L. D. Marks, R. P. Van Duyne, *J. Phys. Chem. C* **2010**, *114*, 12511.
- [18] M.-Q. Yang, C. F. Tan, W. Lu, K. Zeng, G. W. Ho, *Adv. Funct. Mater.* **2020**, *30*, 2004460.
- [19] K. Sapkota, P. Chaudhary, S. S. Han, *RSC Adv.* **2018**, *8*, 31311.
- [20] a) W.-J. Ong, L.-L. Tan, S.-P. Chai, S.-T. Yong, A. R. Mohamed, *Nanoscale* **2014**, *6*, 1946; b) J. Wang, P. Zhang, X. Li, J. Zhu, H. Li, *Appl. Catal., B* **2013**, *134*, 198.
- [21] C. K. N. Peh, M. Gao, G. W. Ho, *J. Mater. Chem. A* **2015**, *3*, 19360.
- [22] M. Kim, J.-H. Lee, J.-M. Nam, *Adv. Sci.* **2019**, *6*, 1900471.
- [23] W. Melitz, J. Shen, A. C. Kummel, S. Lee, *Surf. Sci. Rep.* **2011**, *66*, 1.
- [24] a) C. K. Sun, F. Vallée, L. H. Acioli, E. P. Ippen, J. G. Fujimoto, *Phys. Rev. B* **1994**, *50*, 15337; b) E. Ringe, M. R. Langille, K. Sohn, J. Zhang, J. Huang, C. A. Mirkin, R. P. Van Duyne, L. D. Marks, *J. Phys. Chem. Lett.* **2012**, *3*, 1479.
- [25] a) S. Link, M. A. El-Sayed, *Annu. Rev. Phys. Chem.* **2003**, *54*, 331; b) G. Baffou, R. Quidant, *Chem. Soc. Rev.* **2014**, *43*, 3898.